

Training CNN Classifiers for Semantic Segmentation using Partially Annotated Images: with Application on Human Thigh and Calf MRI

Chun Kit Wong, Stephanie Marchesseau, Maria Kalimeri, Tiang Siew Yap, Serena S. H. Teo, Lingaraj Krishna, Alfredo Franco-Obregón, Stacey K. H. Tay, Chin Meng Khoo, Philip T. H. Lee, Melvin K. S. Leow, John J. Totman, and Mary C. Stephenson

Abstract—Objective: Medical image datasets with pixel-level labels tend to have a limited number of organ or tissue label classes annotated, even when the images have wide anatomical coverage. With supervised learning, multiple classifiers are usually needed given these partially annotated datasets. In this work, we propose a set of strategies to train one single classifier in segmenting all label classes that are heterogeneously annotated across multiple datasets without moving into semi-supervised learning. **Methods:** Masks were first created from each label image through a process we termed presence masking. Three presence masking modes were evaluated, differing mainly in weightage assigned to the annotated and unannotated classes. These masks were then applied to the loss function during training to remove the influence of unannotated classes. **Results:** Evaluation against publicly

available CT datasets shows that presence masking is a viable method for training class-generic classifiers. Our class-generic classifier can perform as well as multiple class-specific classifiers combined, while the training duration is similar to that required for one class-specific classifier. Furthermore, the class-generic classifier can outperform the class-specific classifiers when trained on smaller datasets. Finally, consistent results are observed from evaluations against human thigh and calf MRI datasets collected in-house. **Conclusion:** The evaluation outcomes show that presence masking is capable of significantly improving both training and inference efficiency across imaging modalities and anatomical regions. Improved performance may even be observed on small datasets. **Significance:** Presence masking strategies can reduce the computational resources and costs involved in manual medical image annotations.

This work was partially funded by the NUHS Imaging Core Grant [NMRC/CG/M009/2017_NUH/NUHS]. MRI acquisition of our calf-tissue dataset was funded by Nestlé Institute of Health Sciences (NIHS) and the EpiGen Consortium. (*Corresponding author: Chun Kit Wong.*)

Chun Kit Wong, Tiang Siew Yap, Serena S. H. Teo, and Mary C. Stephenson are with the Clinical Imaging Research Centre, Yong Loo Lin School of Medicine, National University of Singapore (email: wongck@nus.edu.sg).

Stephanie Marchesseau was with the Clinical Imaging Research Centre, Yong Loo Lin School of Medicine, National University of Singapore. She is now with Savana Medica, Madrid, Spain.

Maria Kalimeri and John J. Totman were with the Clinical Imaging Research Centre, Yong Loo Lin School of Medicine, National University of Singapore.

Lingaraj Krishna is with the Department of Orthopaedic Surgery, National University Hospital, National University Health System, Singapore.

Alfredo Franco-Obregón is with (1) Department of Surgery, Yong Loo Lin School of Medicine, National University of Singapore, (2) Biologic Currents Electromagnetic Pulsing Systems Laboratory, BICEPS, National University of Singapore, and (3) Institute for Health Innovation & Technology, iHealthtech, National University of Singapore

Stacey K. H. Tay is with (1) Department of Paediatrics, Yong Loo Lin School of Medicine, National University of Singapore, and (2) KTP-National University Childrens Medical Institute, National University Health System, Singapore

Chin Meng Khoo is with (1) Department of Medicine, Yong Loo Lin School of Medicine, National University of Singapore, and (2) Department of Medicine, National University Health System, Singapore

Philip T. H. Lee is with the Agency for Science, Technology, and Research, Singapore

Melvin K. S. Leow is with (1) Clinical Nutrition Research Centre, Singapore Institute for Clinical Sciences, Agency for Science, Technology, and Research, Singapore, (2) Cardiovascular and Metabolic Disorders Program, Duke-National University of Singapore Medical School, Singapore, (3) Lee Kong Chian School of Medicine, Nanyang Technological University, Singapore, and (4) Department of Endocrinology, Tan Tock Seng Hospital, Singapore

Index Terms—CNN, deep learning, musculoskeletal, partially annotated, segmentation

I. INTRODUCTION

Medical image analysis has recently been dominated by deep learning (DL) methods [1]. This is especially true for semantic segmentation, where most state-of-the-art algorithms involve the use of Convolutional Neural Network (CNN). For instance, the U-Net architecture [2] has been widely used in semantic segmentation to generate 2D pixel-level label map. Numerous extensions of the architecture have since been proposed, such as the 3D U-Net [3] and V-Net [4].

While DL has been successful in extracting highly implicit pattern from the data, performance in its biomedical application is often limited by availability of annotated data itself [1]. Specifically in semantic segmentation, datasets manually annotated with pixel-level label map are often small, due to intense labour and high technical expertise requirement on the annotator. This has led to development of alternative annotation and training strategies, many of which extend concepts from weakly- and semi-supervised learning [5] to train classifiers using both labelled and unlabelled images [6]. Weak labels such as point, bounding-box, or image level labels [7]–[9] may also be utilized in addition to the strong, pixel-level labels. One specific implementation, commonly known as self-supervised learning, uses the Expectation-Maximization (EM) algorithm [10] to alternate between predicting strong

labels for weakly- and un-labelled feature images, and optimizing classifiers using both manually-annotated and the predicted strong labels as ground-truth [5]. Since weakly- and un-labelled biomedical images are often much easier to collect [11], larger dataset can be obtained with a reduced labour budget. However, such approaches come with their own drawbacks [12], [13], and may not work better than the fully supervised approach.

Recently, a number of works on multi-organ analysis have been published [14], with many taking DL approaches, as expected [15]–[19]. In such contexts, there exists an additional form of the data scarcity problem that tends to get neglected. Multi-organ semantic segmentation datasets, such as the 20-class VISCERAL [20] or the 19-class "Computational Anatomy" [18] datasets, remain relatively rare as compared to single-organ datasets. More typically, only a limited number of organs are annotated, even when the acquired feature images may cover multiple organs. With only single-organ datasets available, multiple classifiers have to be trained to segment all organs of interest if a fully supervised learning setting is desired. This potentially leads to inefficiencies, especially among label classes with similar appearance, since the classifiers have to separately learn a redundant set of features. Furthermore, to obtain predictions for all label classes, multiple inferences have to be made separately with the classifiers, which is less optimal especially for inference-on-the-edge applications.

In this work, we propose a method to train one multi-organ classifier utilizing single-organ datasets under supervised learning. This is done by first merging the single-organ datasets (with proper class label mapping function) into a larger, partially labelled multi-organ dataset. We then developed a few strategies to prevent un-annotated label classes from contributing to the loss function, which we term collectively as *presence masking*. These strategies are evaluated using openly available Computed Tomography (CT) datasets from the Medical Segmentation Decathlon 2018 (MSD2018) [21]. Here, we showed that a multi-organ classifier trained using our method is capable of delivering performance on-par with single-organ classifiers. Additional evaluations are performed under small training dataset scenario, simulated by shrinking the MSD2018 dataset, with results indicating that the multi-organ classifier actually outperforms single-organ classifiers among label classes with similar appearance.

To further verify performance of our proposed method, we applied the presence masking strategies on human thigh and calf Magnetic Resonance (MR) images. Much like other applications, annotated label maps of human thigh and calf are often needed for quantitative musculoskeletal analysis [22]–[25]. Since annotated thigh and calf datasets with open access are rarely available, most publications resorted to dedicatedly annotating their own images for classifier training [26], [27]. Here, we show that it is equivalent to using partially labelled images from various sources, even if they're heterogeneous in many way (healthy/pathologic subjects, imaging protocol, label class annotated, etc).

The rest of this paper is organized as follows: Section II provides detailed descriptions of the methodology. In particular, Section II-B explains our proposed presence masking strate-

gies to handle the situation whereby an organ/tissue potentially exists on the feature image but is missing from the label map. Section III describes technical details behind the evaluation experiments. In total, three experiments are performed, with the corresponding results shown and discussed under Section IV. Sections III-D.1 and IV-A compares performance of the proposed multi-organ classifiers with single-organ classifiers in segmenting the MSD2018 dataset. Sections III-D.2 and IV-B further evaluate the multi-organ classifiers' performance with small training datasets, simulated by shrinking the original training dataset into smaller proportions. Sections III-D.3 and IV-C applies the validated method on segmenting MR images of the human thigh and calf. Section IV-D discusses about potential integrations of the proposed presence masking strategies with existing DL methodologies.

II. METHODOLOGY

A. Notation

CT and MR feature image is denoted $\mathbf{x} = \{x_m\}$, $m \in \{1, \dots, M\}$, with x_m being the pixel value at location m . The corresponding ground-truth label map is denoted $\mathbf{y} = \{y_m\}$, with $y_m = c$, $c \in \{0, \dots, C\}$ indicates that x_m 's ground-truth class is c , which can either be the background class 0 or any of the C foreground classes.

CNN classifier is denoted $f(\mathbf{x}, \boldsymbol{\theta})$, with $\boldsymbol{\theta}$ parametrizing all model parameters. It is assumed that the final layer of the classifier is the softmax function. Pixel-wise, per-class probability that x_m belongs to class c is denoted $\mathbf{p} = \{p_m^c\}$, with the corresponding predicted label map denoted as $\hat{\mathbf{y}} = \{\hat{y}_m\}$. For both y_m and \hat{y}_m , the c -superscripted counterpart denotes the label map in one-hot representation:

$$y_m^c = \begin{cases} 1 & \text{if } y_m = c \\ 0 & \text{else} \end{cases} \quad (1)$$

A dataset $D = \{(\mathbf{x}, \mathbf{y})_n\}$, $n \in \{1, \dots, N\}$ with N image pairs (\mathbf{x}, \mathbf{y}) is completely labelled when each of the C foreground classes are fully annotated on \mathbf{y} whenever it appears on \mathbf{x} . Formally, this implies that $y_m = c$ if and only if x_m should be assigned the ground-truth label class c , for every class $c \in \{0, \dots, C\}$. Conversely, in a partially labelled dataset, $y_m \neq c$ does not necessarily indicate that x_m should not be assigned to class c . For example, when a liver dataset is combined with a spleen dataset (with proper mapping such that $c = 1$ represents liver while $c = 2$ represents spleen), the resultant dataset is partially labelled. Images originating from the liver dataset may contain pixels x_m corresponding to spleen, but are assigned the background class label (i.e. $y_m = 0$) since spleen is not annotated in its parent dataset. In another words, $c \in \{0, 2\}$ shall be ignored in \mathbf{y} .

B. Presence masking for partially labelled dataset

Fig. 1 depicts the workflow in supervised semantic segmentation. An overview of supervised semantic segmentation can be found under Section S1-A in the supplementary material. Independent of the choice of loss function, the workflow described under Section S1-A works only when the training

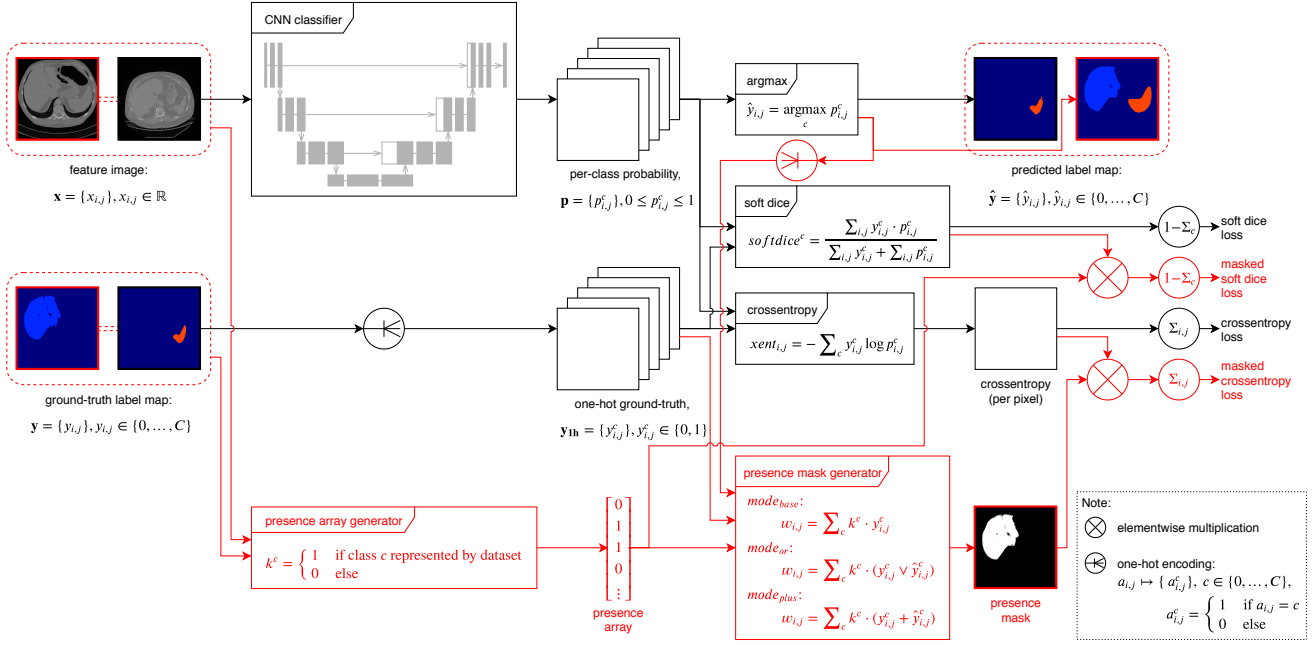


Fig. 1: Workflow in training CNN classifier for semantic segmentation. Black components indicate steps taken when training images are completely segmented, while red components indicate additional steps when they are partially segmented. Note that (i, j) is used to represent pixel location in the 2D images, in place of the dimension-independent m used in the main text.

dataset is completely labelled. With partially labelled training dataset, classes not annotated should be masked out while computing the loss function $J(\theta)$. This leads to our proposed presence masking strategies.

1) *Presence masking the dice losses:* To begin with, a dataset-level presence array $\mathbf{k} = \{k^c\}$, $k^c = \{0, 1\}$ is defined for each (\mathbf{x}, \mathbf{y}) pairs, with $k^c = 0$ indicating that class c is not annotated manually in the dataset. In another words, any presence of class c in \mathbf{y} is invalidated. This can then be directly applied onto the class-aggregation term in the dice losses (see Eqs. (S4) and (S6) in the supplementary material) to obtain the masked soft dice loss:

$$J_{dice_{soft}}(\theta) = \frac{\sum_c k^c \cdot (1 - \text{softdice}^c)}{\sum_c k^c} \quad (2)$$

or the masked log dice loss:

$$J_{dice_{log}}(\theta) = \frac{\sum_c k^c \cdot (-\log \text{softdice}^c)}{\sum_c k^c} \quad (3)$$

2) *Presence masking the crossentropy loss:* Crossentropy loss, however, requires extra steps. For class c where $k^c = \text{true}$, false positive errors occur at location m where $y_m \neq c$ and $\hat{y}_m = c$ hold. When $y_m \neq c$, $k^c \cdot y_m^c = 0$ regardless of k^c . This means that false positive errors are potentially ignored if \mathbf{k} is applied directly to the class aggregation term in the crossentropy loss. To mitigate this, a presence mask $\mathbf{w} = \{w_m\}$, $m \in \{1, \dots, M\}$ can be defined and applied to the pixel aggregation term instead:

$$J_{xent}(\theta) = -\sum_m w_m \sum_c y_m^c \log p_m^c \quad (4)$$

We propose multiple way, which we denote as *mode*, to construct \mathbf{w} :

- *mode_{base}*: set $w_m = 1$ at every location m where $y_m = c$ and $k^c = 1$, and $w_m = 0$ wherever $y_m = c$ and $k^c = 0$. This can be formulated compactly as:

$$w_m = \sum_c k^c \cdot y_m^c \quad (5)$$

- *mode_{or}*: same as *mode_{base}*, but extended to also include every location m where $\hat{y}_m = c$. In other words, take the elementwise-or between \mathbf{y} and $\hat{\mathbf{y}}$, instead of \mathbf{y} alone:

$$w_m = \sum_c k^c \cdot (y_m^c \vee \hat{y}_m^c) \quad (6)$$

- *mode_{plus}*: same as *mode_{or}*, but take the elementwise-sum between \mathbf{y} and $\hat{\mathbf{y}}$ instead of elementwise-or:

$$w_m = \sum_c k^c \cdot (y_m^c + \hat{y}_m^c) \quad (7)$$

Effectively, *mode_{base}* is equivalent to generating the presence mask \mathbf{w} by binary thresholding the ground truth label map \mathbf{y} , such that only foreground class c with $k^c = 1$ in the presence array \mathbf{k} are mapped to 1 in \mathbf{w} . However, this naive approach does not resolve the issue mentioned at the beginning of this section, since it also ignores false positive errors when \mathbf{y} is partially labelled. To avoid masking out false positive errors, the predicted label map $\hat{\mathbf{y}}$ has to be incorporated while constructing \mathbf{w} . Among many possible approaches, this could be achieved by computing either the elementwise-or (*mode_{or}*) or elementwise-sum (*mode_{plus}*) between \mathbf{y} and $\hat{\mathbf{y}}$. Essentially, these two modes only differ in terms of how the true positive and false positive/negative pixels are weighted (see Fig. 2):

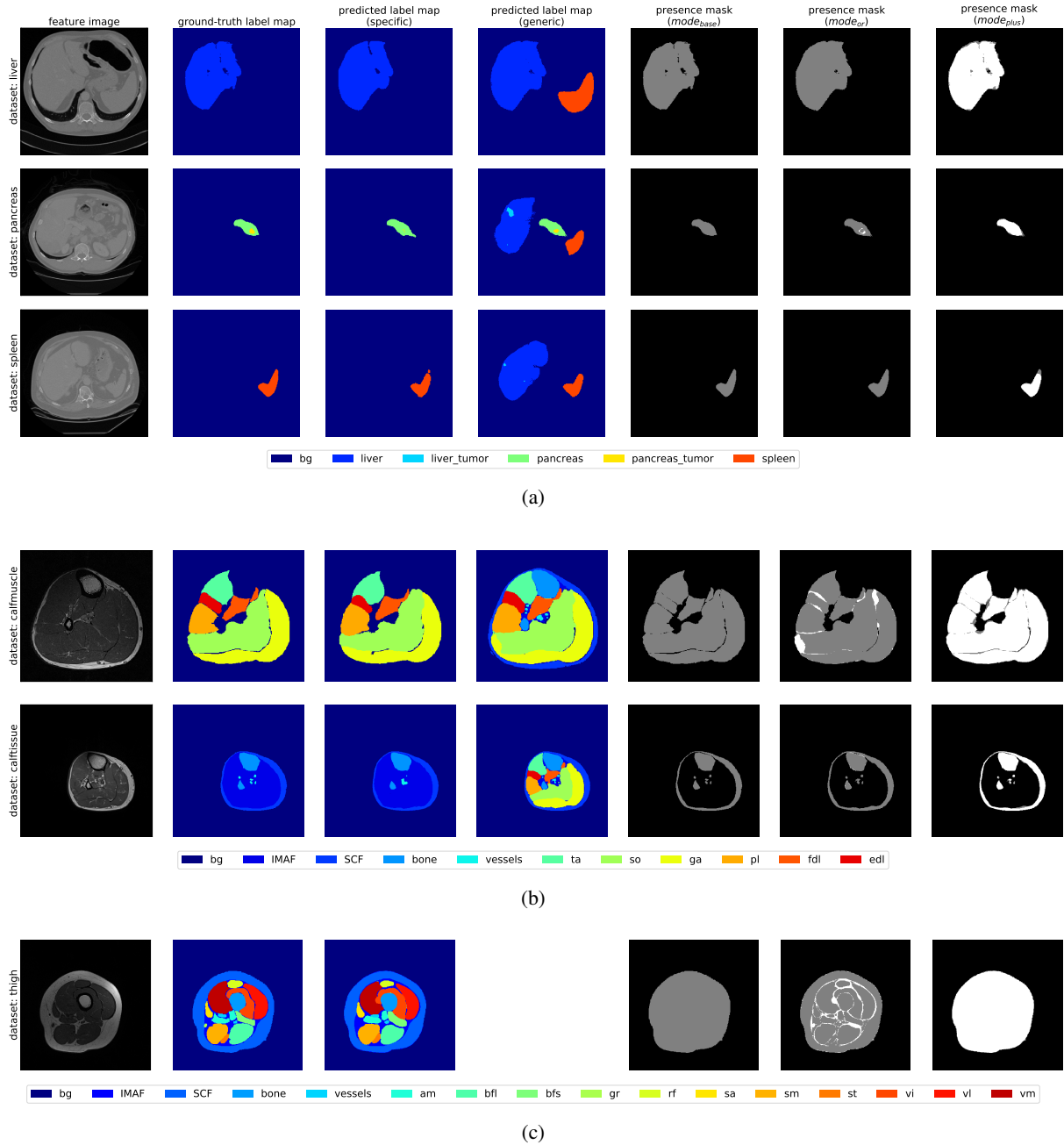


Fig. 2: Screenshots of feature image and label map from (a) MSD2018, (b) calf, and (c) thigh datasets, together with example predictions by the specific- and generic-classifiers (see Section III). Presence mask in different modes are generated using the ground-truth label maps and the corresponding generic-classifier’s predictions. Note how the generic-classifiers predict all label classes present in the entire (partially labelled) dataset. Generic-classifier’s prediction for the thigh dataset is omitted since it is completely labelled.

$mode_{or}$ assigns equal weightage to all these pixels, while $mode_{plus}$ assigns heavier weightage to the true positive pixels.

To avoid any confusion, note the difference between presence array \mathbf{k} and the image-level annotation commonly used in a weakly-supervised setting [7]. Presence array indicates whether or not a label class c is represented in the dataset. When $k_c = true$, even when $y_m \neq c$ for all m , it indicates a true negative situation. Any prediction that says $\hat{y}_m = c$

should be treated as a false positive error. On the other hand, a positive image-level annotation for class c indicates that if the pixel-level label map \mathbf{y} exists, $y_m = c$ can be observed for at least one location m .

3) Presence masking and completely labelled image: While our presence masking strategies are developed to handle partially labelled images, it is also applicable to completely labelled images, which is essentially the special case where

$k_c = true$ for all label class c . Under this special case, the masked dice losses (Eqs. (2) and (3)) simply become the unmasked versions scaled by a constant value $1/\sum_c k^c$. Crossentropy loss masked with $mode_{base}$ presence mask also converges back to the unmasked version. Presence mask under $mode_{or}$ and $mode_{plus}$, however, can then be seen as an attempt to improve the loss functions, by weighting each pixel differently. Hence, this should be taken into consideration while performing any performance evaluations (see Sections III-D.1 and IV-A).

III. EXPERIMENTAL EVALUATIONS

To facilitate discussion, we denote classifiers trained with completely labelled single-organ dataset as *specific*-classifiers. Alternatively, those trained with partially labelled multi-organ dataset are denoted *generic*-classifiers (see Fig. 2). Classifiers are also addressed based on the loss function and mode of presence mask (where included). For example, a $xent_{or} + 0.1 * dice_{soft}$ classifier refers to the classifier trained with loss function $J_{xent}(\theta) + 0.1 * J_{dice_{soft}}(\theta)$, where the presence mask applied pixel-wise to the crossentropy loss is in $mode_{or}$.

A. Datasets

All evaluations in this work leverage on annotated image pairs (x, y) from two main sources. For reproducibility, the proposed method under Section II was evaluated with image pairs (x, y) from the MSD2018; specifically the liver (131 pairs), pancreas (281 pairs), and spleen (41 pairs) datasets amongst the 10 available datasets. All 3 datasets contain CT feature images of the abdominal region. In addition to healthy tissues, tumors were also annotated in both liver and pancreas datasets. Images from these datasets were merged into one large partially-labelled dataset with proper class-mapping scheme.

MR feature images of human thigh and calf were acquired at the Clinical Imaging Research Centre, National University of Singapore. These MR images were acquired using turbo spin echo (TSE) sequence and Siemens Magnetom 3T Prisma or TrioTim systems. Ground-truth label maps were manually annotated by certified radiographers using MITK (v2015.05.02) [28]. The calf dataset is partially labelled, and comprised of two sub-datasets: a calf-muscle dataset containing 22 left calves acquired from healthy subjects, with 6 muscle groups annotated, and a calf-tissue dataset containing 84 left and right calves acquired simultaneously from 42 subjects, with 3 tissue classes (bone, blood vessels, subcutaneous fat (SCF)) annotated. On the other hand, the thigh dataset is comprised of completely labelled (x, y) pairs with 4 tissue classes (bone, blood vessels, SCF, and intermuscular adipose fat (IMAF)) and 11 muscle group classes annotated, with 40 thighs acquired from 20 double-visit surgical subjects. Full detail of the datasets can be found in the supplemented Table S1.

B. Pre- and post-processing

For the train-test cycle, all images from the MSD2018 dataset were resampled with bilinear interpolation to match the

standardized $1.5 \times 1.5 \text{mm}^2$ in-plane resolution and 3.5mm slice thickness. Thigh images were resampled to $0.78 \times 0.78 \text{mm}^2$ in-plane resolution, with no resampling in the slice direction. These were then cropped/zero-padded to form 256×256 slices. On the other hand, images from the calf-tissue dataset were cropped into single calves and combined with the calf-muscle dataset, before all images were resampled to $0.54 \times 0.54 \text{mm}^2$ in-plane resolution and cropped/zero-padded to form 320×320 slices.

At inference time, feature images x were similarly resampled to the standardized resolution. Predicted label maps \hat{y} from the trained classifiers were then resampled (with nearest-neighbour interpolation) to match the original resolution and array size. For all evaluation results reported in the following sections, dice scores were calculated between y and \hat{y} in their original resolution and array size.

Note that the images were resampled aggressively to expedite the train-test cycle, as well as to reduce computational cost needed. However, this had also inevitably led to interpolation error on the final result. Performance is expected to improve when all images are processed in their original resolution.

C. Training details

Neural networks were implemented with Tensorflow (v1.4) in Python. All CNN classifiers used in this work were instances of the 2D U-Net model [2] with additional batch normalization layers after every convolution and deconvolution layers to improve robustness against variance within each mini-batch [29].

Much of the training hyperparameters were empirically fixed. Network parameters θ were initialized with Xavier initialization [30] and optimized using Adam optimizer [31]. A default learning rate of 10^{-4} was chosen, and was reduced to 10^{-5} only if the training failed to progress. Patch-based approaches were omitted for simplicity. All classifiers were trained until convergence in a cluster equipped with Intel E5-2690v3 and NVIDIA Tesla K40.

Classifiers were trained using mini-batches of (x, y) from D_{train} , with 15 image pairs per batch. To improve training stability of the generic-classifiers, these image pairs were drawn from their parent dataset using stratified sampling. Each batch was a mixture of (x, y) from each parent dataset at a constant proportion. Then, for both specific- and generic-classifiers, half of the image pairs were labelled with at least one foreground class, while the other half did not contain any foreground labels.

D. Experiment configurations

1) *Specific- versus generic-classifiers*: The proposed presence masking strategies in Section II-B were first evaluated using the MSD2018 dataset, with 80:20 split into train D_{train} and test D_{test} sets. 11 combinations of loss function and presence array/mask were investigated. For each combination, 3 specific-classifiers were trained using the completely labelled liver, pancreas, and spleen datasets respectively, and 1 generic-classifier was trained using the merged partially labelled dataset. Since the presence masking strategies can potentially

affect the specific-classifiers' performance (see Section II-B.3), all 11 combinations were applied to both the specific- and generic-classifiers to ensure a fair comparison. The entire setup was then repeated in 3 orthogonal slicing directions (i.e. axial, coronal, and sagittal) to identify the best performing direction for next experiment (Section III-D.2).

2) *Training with small datasets*: Performance of the presence masking strategies were then evaluated with small training dataset to investigate the impact of training size on the specific- and generic-classifier approaches. From the original 80:20 train-test split, the training dataset was gradually halved to form smaller datasets 40%, 20%, 10%, 5%, and 2.5% of the original datasets. The specific- and generic-classifiers were then trained with each of the reduced training datasets. Loss functions (5 choices for both specific- and generic-classifier) as well as slicing direction (i.e. axial) were all chosen based on results from Section III-D.1.

3) *Application on human thigh & calf datasets*: Finally, the presence masking strategies were further evaluated using the human thigh and calf datasets. To compliment the evaluation against the MSD2018 dataset (i.e. Section III-D.1), all 11 loss function and presence array/mask combinations were again investigated with 80:20 train-test split. To ensure a fairer evaluation, an additional condition was imposed such that if multiple images exist for one subject, these images must all belong to either the training or the test set, but not both. For each combination, 2 specific-classifiers were trained using the calf-tissue and calf-muscle datasets respectively, while 1 generic-classifier was trained using the combined partially labelled calf dataset. On the other hand, only 1 specific-classifier was trained using the thigh dataset since it is completely labelled. Since IMAF was not labelled within the entire calf dataset, a workaround was implemented: within the calf-tissue dataset, the entire region medial from SCF was labelled as IMAF (see Fig. 2b), but the element corresponding to IMAF was marked as False in the presence array. This allowed the classifier to learn labeling undefined region within vicinity of the muscle groups as IMAF instead of background.

IV. RESULTS AND DISCUSSIONS

A. Evaluation 1: specific- versus generic-classifiers

Results shown in Table I indicate that soft dice loss failed altogether for both the specific- and generic-classifier. This was mitigated among the specific-classifiers when empty slices (i.e. slices without any foreground label) were removed from D_{train} , as seen from the row with loss function $dice_{soft}(w/o\ empty)$ in Table I. However, without exposure to empty slices the classifiers then suffered from high false-positive errors, resulting in poorer precision and dice performance on D_{test} . This was resolved by using combinations of crossentropy and soft dice as the loss function (see Eq. (S7) in the supplementary material).

As expected following arguments under Section II-B, Table I shows that among generic-classifiers with a crossentropy component in the loss function, inclusion of the presence mask generated in $mode_{or}$ and $mode_{plus}$ resulted in improved performance as compared to $mode_{base}$ (see Fig. S1 in the

supplementary material for visualization). This was not observed among the specific-classifiers, which indicates that the benefit of applying the presence masking strategies in training the specific-classifier (see Section II-B.3) is not obvious. In another words, special handling of the false-positive errors with $mode_{or}$ and $mode_{plus}$ did not significantly improve classifiers trained with completely labelled dataset.

It worth noting that both specific- and generic-classifier failed to segment tumor classes properly (see Table S2 in the supplementary material). In fact, their performance in segmenting pancreas was also mediocre at best. This is not unexpected, since these label classes are classically challenging, and tend to require handlings more sophisticated than the generic crossentropy and soft dice loss [32], [33]. Since this work only aims to compare performance between the specific- and generic-classifier under the same setting, improving performance of difficult label classes is omitted.

1) *Performance*: Predicted label masks can be generated in a few ways during inference time. Where maximal accuracy is desired, this can be done using multiple best performing generic-classifiers. From the bold entries under each column of Table I, this corresponds to the $xent_{plus}$ (best for liver) and $xent_{plus} + 0.1 * dice_{soft}$ (best for pancreas/spleen) generic-classifier. Multiple label maps are then predicted using these generic-classifiers, followed by masking out label classes where the corresponding generic-classifier does not perform best. Finally, a label map can be obtained by merging these masked label maps. Note that this is very similar to the conventional specific-classifiers approach, except for the extra masking step since label maps predicted by the generic-classifiers are completely labelled. Alternatively, a more efficient approach is described under Section IV-A.2.

Table I indicates that dice score achieved by the best performing generic-classifier marginally outperformed the best specific-classifiers. This suggests that generating label maps with generic-classifier approach potentially yields better performance. However, depending on applications, this marginal performance gain may not justify the efficiency of inferencing with one single generic-classifier instead (see Section IV-A.2).

2) *Efficiency*: At inference time, it is motivating to predict the entire label masks with one single generic-classifier, rather than merging multiple predictions from the best performing generic-classifiers as described under Section IV-A.1. Ideally, the selected generic-classifier should perform reasonably well across each label class, so as to minimize sacrifice on performance while attempting to improve efficiency. This can be achieved with various selection criterion, such as by choosing the generic-classifier which yields the highest average dice score. From Table I, this corresponds to the $xent_{plus} + 0.1 * dice_{soft}$ generic-classifier (0.8313 on average), which performed slightly worse (0.8944) than the best performing generic-classifier (0.9097) in liver, but could nonetheless promote a good trade-off between performance per-class and the number of inferences required per-image. This could be particularly useful when computational budget during inference is limited.

On the other hand, in terms of training speed, Fig. 3 indicates that convergence of the generic-classifier's training

TABLE I: Dice performance of the specific- and generic-classifiers on the test set D_{test} , tabulated against loss function used in training the classifiers. Dice scores in bold correspond to the best performing classifier in each label class. Only classifiers trained with axial slices are shown, which is discovered to be the best performing slicing direction. Dice performance on tumor classes are also omitted. See Table S2 in the supplementary material for full result.

| plane | label_class | average | | liver | | pancreas | | spleen | |
|-------|-----------------------------------|---------------|---------------|---------------|---------------|---------------|---------------|---------------|---------------|
| | classifier_type | generic | specific | generic | specific | generic | specific | generic | specific |
| | loss_function | | | | | | | | |
| axial | $dice_{soft}$ | 0.0014 | 0.0000 | 0.0000 | 0.0000 | 0.0043 | 0.0000 | 0.0000 | 0.0000 |
| | $dice_{soft}(w/o\ empty)$ | 0.4313 | 0.7283 | 0.0000 | 0.8606 | 0.5254 | 0.5153 | 0.7684 | 0.8089 |
| | $dice_{log}$ | 0.1959 | 0.5850 | 0.2278 | 0.8244 | 0.2672 | 0.1606 | 0.0925 | 0.7702 |
| | $xent_{base}$ | 0.0814 | 0.8319 | 0.1717 | 0.9064 | 0.0475 | 0.6919 | 0.0251 | 0.8973 |
| | $xent_{base} + 0.1 * dice_{soft}$ | 0.6886 | 0.8135 | 0.6047 | 0.8857 | 0.6408 | 0.6641 | 0.8202 | 0.8907 |
| | $xent_{base} + dice_{log}$ | 0.7637 | 0.7952 | 0.8423 | 0.8915 | 0.5933 | 0.5963 | 0.8556 | 0.8977 |
| | $xent_{or}$ | 0.8185 | 0.7792 | 0.9049 | 0.9045 | 0.6845 | 0.6209 | 0.8662 | 0.8121 |
| | $xent_{or} + 0.1 * dice_{soft}$ | 0.8148 | 0.8299 | 0.8980 | 0.9023 | 0.6860 | 0.6869 | 0.8605 | 0.9005 |
| | $xent_{or} + dice_{log}$ | 0.8033 | 0.7799 | 0.9018 | 0.8976 | 0.6419 | 0.6222 | 0.8662 | 0.8198 |
| | $xent_{plus}$ | 0.8202 | 0.8107 | 0.9097 | 0.9080 | 0.6619 | 0.6735 | 0.8890 | 0.8506 |
| | $xent_{plus} + 0.1 * dice_{soft}$ | 0.8313 | 0.8210 | 0.8944 | 0.9063 | 0.6985 | 0.6716 | 0.9009 | 0.8851 |
| | $xent_{plus} + dice_{log}$ | 0.7979 | 0.8125 | 0.8989 | 0.9060 | 0.6528 | 0.6493 | 0.8421 | 0.8821 |

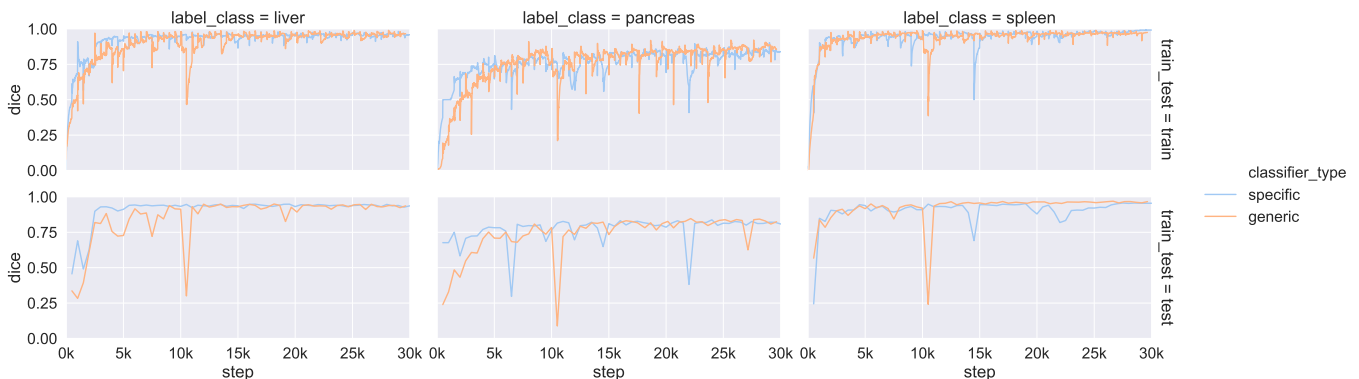


Fig. 3: Training curves of the specific- and generic-classifier trained with loss function $xent_{or} + 0.1 * dice_{soft}$. Train and test dice scores are plotted against training step elapsed for each label class.

and test dices closely followed the specific-classifier’s. This lag was more prevailing for label class (i.e. pancreas) with distinct appearance from other classes (i.e. liver and spleen). Nonetheless, training a single generic-classifier is still arguably more efficient without exceeding the combined duration needed for training 3 specific-classifiers to convergence. In other words, training $\mathcal{O}(1)$ generic-classifiers to segment n label classes is asymptotically less expensive than training $\mathcal{O}(n)$ specific-classifiers.

B. Evaluation 2: training with small datasets

As a sanity check, Fig. 4 shows that performance of the classifiers improved with larger D_{train} . This observation holds true for both specific- and generic-classifier, which is as expected.

1) *Performance:* Fig. 4a shows that among label classes with similar appearance (i.e. liver and spleen), performance of the best generic-classifier often outperformed the best specific-classifier. This was increasingly apparent as size of D_{train} shrinks, particularly for label class from the smaller dataset (i.e. spleen). Label classes with distinct appearance

(i.e. pancreas), however, did not benefit from this performance boost.

This observed behavior is very likely linked to transfer learning, where classifiers are pre-trained using large dataset prior to fine-tuning for target application with smaller dataset. While in this case it is likely that the spleen specific-classifier’s performance can be boosted by simply pre-training the classifier with liver dataset, it is not so straightforward when, say, a kidney dataset is simultaneously available and can potentially improve the spleen specific-classifier’s performance too. The generic-classifier approach extends transfer learning’s capability such that the pre-training step leverages on multiple dataset simultaneously, i.e. without manual grouping of label classes based on their appearance.

2) *Efficiency:* With smaller D_{train} sizes, the strategy described in Section IV-A.2 to improve inference efficiency failed, as shown in Fig. 4b. Dice score achieved by the selected, best-on-average generic-classifiers at each D_{train} size were often low as compared to the best generic-classifiers. This could potentially be resolved with minor amendment to the aforementioned strategy. For example, the generic-

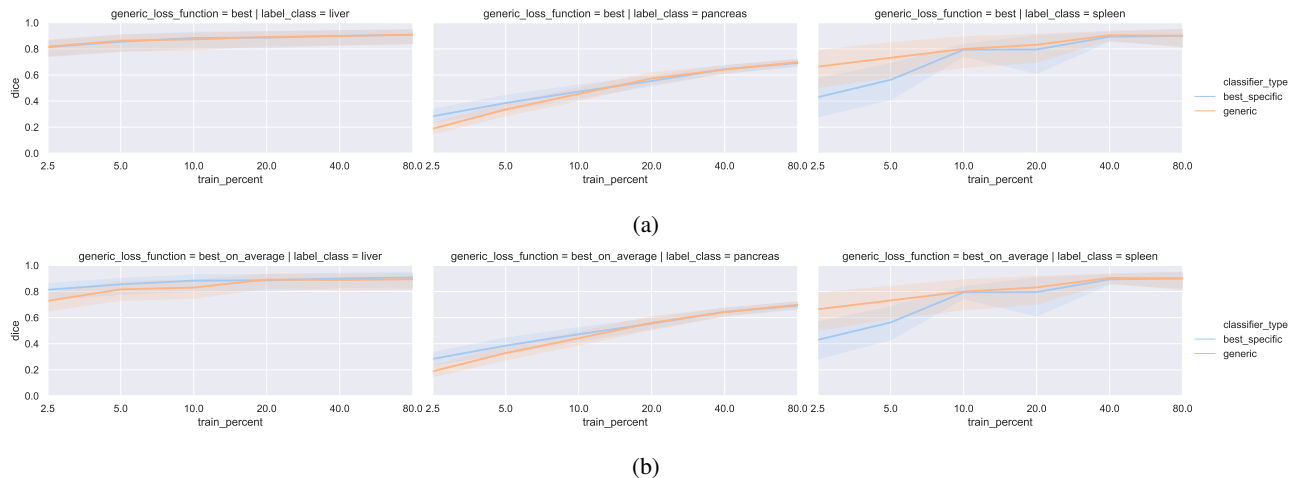


Fig. 4: Visualization of results from Section IV-B. See Table S3 in the supplementary material for full result. (a) Dice score achieved by the best performing specific- and generic-classifier are plotted against size of D_{train} (i.e. bold entries in Table S3); (b) same as a but with the best-on-average generic-classifiers instead. These are generic-classifiers scoring the highest dice score on-average for each D_{train} size, i.e. from Table S3, $xent_{or} + dice_{log}$ trained generic-classifiers at 2.5%, 5%, and 10% D_{train} , $xent_{plus}$ at 20%, and $xent_{plus} + 0.1 * dice_{soft}$ at 40% and 80%.

classifier performing best on-average in segmenting liver and spleen could be used in conjunction with the best pancreas specific-classifier during inference. Such strategy could still improve overall efficiency of the inference process, but at the expense of additional workflow complexity.

Meanwhile, as shown in the supplemented Table S3, the average dice score between specific- and generic-classifier matched closely for each D_{train} size. Generic-classifiers could potentially be trained with class weightages additionally assigned to each label class in the loss function, such that the generic-classifier’s dice performance is well-balanced across each label class, while maintaining the same average dice score. Since the optimal set of class weightages may require exhaustive tuning, this exploration is omitted here.

C. Evaluation 3: application on human thigh & calf datasets

In general, evaluation results were in good agreement with Section IV-A for the MSD2018 dataset. From Fig. 5, the best-on-average generic-classifier (trained with $xent_{plus} + dice_{log}$) was capable of delivering performance on par with that of the best specific-classifiers, suggesting that efficiency can be improved by inferencing all label classes with the selected generic-classifier only. For certain label classes, the best generic-classifiers performed marginally better than the best-on-average generic-classifier (see the supplemented Table S4). However, these generic-classifiers were not better than the best specific-classifiers in general, which is expected since label classes annotated in the calf-tissue and calf-muscle datasets mostly do not share similar appearance (see Fig. 2b).

It is again observed that $mode_{or}$ and $mode_{plus}$ performed better in general than $mode_{base}$ among the calf generic-classifiers, while such advantage was not observed among the calf and thigh specific-classifiers (see Table S4). Screenshot of label maps predicted by the calf generic-classifiers and thigh

specific-classifiers demonstrate this visually (see Fig. S2 in the supplementary material). Among the calf generic-classifiers, loss functions with $xent_{or}$ or $xent_{plus}$ components were in general better than $xent_{base}$ in isolating the muscle groups from the surrounding IMAF, which was undefined among all ground-truth label map within the calf dataset. Such advantage was not observed among the thigh specific-classifiers.

In terms of absolute performance of the classifiers, dice score was acceptable for most classes given the small size of D_{train} . The only exception was the vessels, which is again a small Region of Interests (ROI) that potentially requires special handling just like tumor classes from the MSD2018 dataset. Additionally, both calf generic- and specific-classifiers were unable to delineate between the 2 muscle groups *peroneus longus* and *extensor digitorum longus* well, but were capable of identifying union of the two label classes, which is represented by $pl + edl$ on Fig. 5 and Table S4.

D. Potential improvements

1) *Compatibility with existing DL methodologies:* This work mainly aims at comparing the performance between existing methods (i.e. specific-classifier) and the proposed generic-classifier approaches, rather than pushing performance of the generic-classifier itself to achieve state-of-the-art semantic segmentation performance. However, it is possible to incorporate the proposed presence masking strategies into many other existing DL methodologies for better performance. This includes adopting the DeepMedic [34] and HyperDense-Net [35] architectures which excelled in brain lesion segmentation, or the Attention U-Net [33] originally proposed for pancreas segmentation. It is also common to see fully-connected Conditional Random Field (CRF) being appended to the network output to improve delineation near ROI boundaries [7], [34]. Additionally, other strategies such as various data augmentation schemes [36] or 2D-to-3D segmentation map by majority

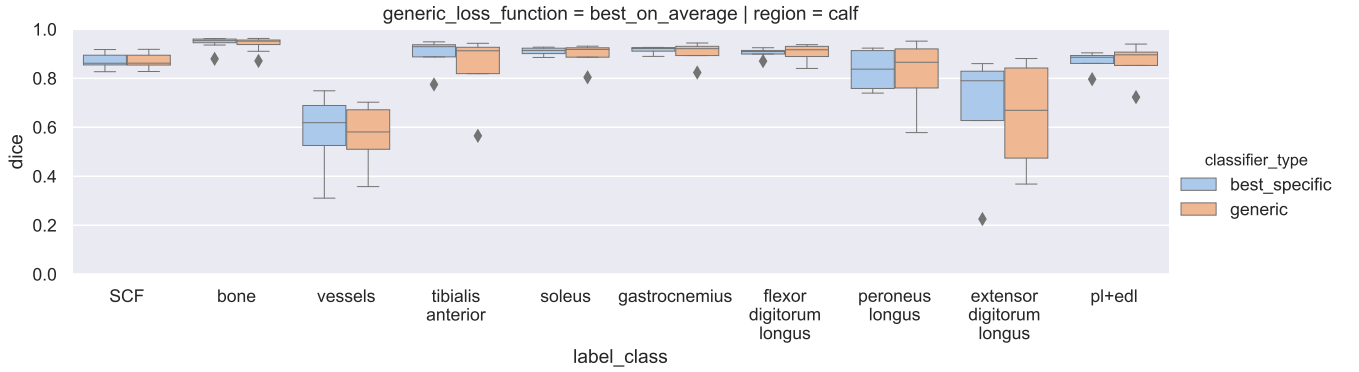


Fig. 5: Visualization of results from Section IV-C, comparing Dice scores achieved by the best specific-classifiers and best-on-average generic-classifiers in segmenting the calf. *pl+edl* represents the pixel-wise union of *peroneus longus* and *extensor digitorum longus*. See Table S4 in the supplementary material for full result.

voting [18] should also be directly applicable.

Note that while the proposed feature array/masks were only validated using dice and crossentropy loss, incorporation to other loss function is trivial in some cases. For instance, the Focal Tversky Loss (FTL) [32] is defined as followed:

$$J_{FTL}(\theta) = \sum_c^C (1 - TI^c)^{1/\gamma} \quad (8)$$

with TI_c being the Tversky index [37] between the ground-truth and predicted label map for label class c . This can be easily modified to incorporate the presence array $\mathbf{k} = \{k^c\}$:

$$J_{FTL}(\theta) = \frac{\sum_c^C k^c (1 - TI^c)^{1/\gamma}}{\sum_c^C k^c} \quad (9)$$

Meanwhile, other loss functions with pixel aggregation terms, such as the Mean Absolute Error (MAE) or L1 loss which is proposed as a noise-robust alternative to crossentropy loss [38]:

$$\begin{aligned} J_{MAE}(\theta) &= - \sum_m^M \sum_c^C |y_m^c - p_m^c| \\ &= - \sum_m^M 2 - 2p_m^{c'}, \quad c' = y_m \end{aligned} \quad (10)$$

can be handled in a fashion similar to Eq. (4):

$$J_{MAE}(\theta) = - \sum_m^M w_m \cdot (2 - 2p_m^{c'}) \quad (11)$$

2) Semi-supervised learning: Technically, the proposed presence masking strategies are much closer to supervised learning than it is to semi-supervised learning. All labels involved in the training are strongly labelled, and classifiers do not learn from the inferred labels. The only exception is perhaps when the classifier makes false positive error at unlabelled pixels, which contribute to the loss function (with presence masks under *mode_{or}* and *mode_{plus}*) even without being annotated with any ground-truth label class. Nevertheless, it is possible to extend the proposed method to support semi-supervised learning scenarios. Since predicted label maps for the partially labelled training images are completely labelled, they can be merged into D_{train} . Classifier can then be iteratively trained until certain termination conditions are met, similar to the EM approach.

ACKNOWLEDGMENT

The computational work for this article was partially performed on resources of the National Supercomputing Centre, Singapore (<https://www.nscg.sg>). The authors also gratefully acknowledge the support of NVIDIA Corporation with the donation of the Titan V GPU used for inferences in this research. All codes are publicly available at <https://github.com/wong-ck/DeepSegment>.

REFERENCES

- [1] G. Litjens, T. Kooi, B. E. Bejnordi, A. A. A. Setio, F. Ciompi, M. Ghafoorian, J. A. van der Laak, B. van Ginneken, and C. I. Sncnez, "A survey on deep learning in medical image analysis," *Medical Image Analysis*, vol. 42, pp. 60 – 88, 2017. [Online]. Available: <http://www.sciencedirect.com/science/article/pii/S1361841517301135>
- [2] O. Ronneberger, P. Fischer, and T. Brox, "U-Net: Convolutional networks for biomedical image segmentation," in *Medical Image Computing and Computer-Assisted Intervention – MICCAI 2015*, N. Navab, J. Hornegger, W. M. Wells, and A. F. Frangi, Eds. Cham: Springer International Publishing, 2015, pp. 234–241.
- [3] Ö. Çiçek, A. Abdulkadir, S. S. Lienkamp, T. Brox, and O. Ronneberger, "3d u-net: Learning dense volumetric segmentation from sparse annotation," in *Medical Image Computing and Computer-Assisted Intervention – MICCAI 2016*, S. Ourselin, L. Joskowicz, M. R. Sabuncu, G. Unal, and W. Wells, Eds. Cham: Springer International Publishing, 2016, pp. 424–432.
- [4] F. Milletari, N. Navab, and S. Ahmadi, "V-Net: Fully convolutional neural networks for volumetric medical image segmentation," *CoRR*, vol. abs/1606.04797, 2016. [Online]. Available: <http://arxiv.org/abs/1606.04797>
- [5] V. Cheplygina, M. de Bruijne, and J. P. Pluim, "Not-so-supervised: A survey of semi-supervised, multi-instance, and transfer learning in medical image analysis," *Medical Image Analysis*, vol. 54, pp. 280 – 296, 2019. [Online]. Available: <http://www.sciencedirect.com/science/article/pii/S1361841518307588>
- [6] X. Zhu and A. B. Goldberg, "Introduction to semi-supervised learning," in *Introduction to Semi-Supervised Learning*, 2009.
- [7] G. Papandreou, L. Chen, K. Murphy, and A. L. Yuille, "Weakly- and semi-supervised learning of a DCNN for semantic image segmentation," *CoRR*, vol. abs/1502.02734, 2015. [Online]. Available: <http://arxiv.org/abs/1502.02734>
- [8] A. Bearman, O. Russakovsky, V. Ferrari, and F. F. Li, "Whats the point: Semantic segmentation with point supervision," vol. 9911, 10 2016, pp. 549–565.
- [9] M. Rajchl, M. C. H. Lee, O. Oktay, K. Kamnitsas, J. Passerat-Palmbach, W. Bai, M. Damodaram, M. A. Rutherford, J. V. Hajnal, B. Kainz, and D. Rueckert, "Deepcut: Object segmentation from bounding box annotations using convolutional neural networks," *IEEE Transactions on Medical Imaging*, vol. 36, no. 2, pp. 674–683, Feb 2017.

- [10] A. P. Dempster, N. M. Laird, and D. B. Rubin, "Maximum likelihood from incomplete data via the em algorithm," *Journal of the Royal Statistical Society. Series B (Methodological)*, vol. 39, no. 1, pp. 1–38, 1977. [Online]. Available: <http://www.jstor.org/stable/2984875>
- [11] T. Lin, M. Maire, S. J. Belongie, L. D. Bourdev, R. B. Girshick, J. Hays, P. Perona, D. Ramanan, P. Dollár, and C. L. Zitnick, "Microsoft COCO: common objects in context," *CoRR*, vol. abs/1405.0312, 2014. [Online]. Available: <http://arxiv.org/abs/1405.0312>
- [12] F. Cozman and I. Cohen, "Risks of semi-supervised learning: How unlabeled data can degrade performance of generative classifiers," in *Semi-Supervised Learning*, O. Chapelle, B. Scholkopf, and A. Zien, Eds. The MIT Press, Sep. 2006, pp. 56–72. [Online]. Available: <https://doi.org/10.7551/mitpress/9780262033589.003.0004>
- [13] A. Singh, R. Nowak, and J. Zhu, "Unlabeled data: Now it helps, now it doesn't," in *Advances in Neural Information Processing Systems 21*, D. Koller, D. Schuurmans, Y. Bengio, and L. Bottou, Eds. Curran Associates, Inc., 2009, pp. 1513–1520. [Online]. Available: <http://papers.nips.cc/paper/3551-unlabeled-data-now-it-helps-now-it-doesnt.pdf>
- [14] J. J. Cerrolaza, M. L. Picazo, L. Humbert, Y. Sato, D. Rueckert, M. ngel Gonzalez Ballester, and M. G. Linguraru, "Computational anatomy for multi-organ analysis in medical imaging: A review," *Medical Image Analysis*, vol. 56, pp. 44 – 67, 2019. [Online]. Available: <http://www.sciencedirect.com/science/article/pii/S1361841518306273>
- [15] H.-C. Shin, M. Orton, D. Collins, S. Doran, and M. Leach, "Stacked autoencoders for unsupervised feature learning and multiple organ detection in a pilot study using 4d patient data," *IEEE transactions on pattern analysis and machine intelligence*, vol. 35, pp. 1930–1943, 08 2013.
- [16] H. Roth, C. Lee, H.-C. Shin, A. Seff, L. Kim, J. Yao, L. Lu, and R. Summers, "Anatomy-specific classification of medical images using deep convolutional nets," vol. 2015, 04 2015.
- [17] Z. Yan, Y. Zhan, Z. Peng, S. Liao, Y. Shinagawa, S. Zhang, D. N. Metaxas, and X. S. Zhou, "Multi-instance deep learning: Discover discriminative local anatomies for bodypart recognition," *IEEE Transactions on Medical Imaging*, vol. 35, no. 5, pp. 1332–1343, May 2016.
- [18] X. Zhou, T. Ito, R. Takayama, S. Wang, T. Hara, and H. Fujita, "Three-dimensional ct image segmentation by combining 2d fully convolutional network with 3d majority voting," in *Deep Learning and Data Labeling for Medical Applications*, G. Carneiro, D. Mateus, L. Peter, A. Bradley, J. M. R. S. Tavares, V. Belagiannis, J. P. Papa, J. C. Nascimento, M. Loog, Z. Lu, J. S. Cardoso, and J. Cornebise, Eds. Cham: Springer International Publishing, 2016, pp. 111–120.
- [19] Y. Wang, Y. Zhou, W. Shen, S. Park, E. Fishman, and A. Yuille, "Abdominal multi-organ segmentation with organ-attention networks and statistical fusion," *Medical Image Analysis*, vol. 55, 04 2018.
- [20] O. Jimenez-del-Toro, H. Miller, M. Krenn, K. Gruenberg, A. A. Taha, M. Winterstein, I. Eggel, A. Foncubierta-Rodriguez, O. Goksel, A. Jakab, G. Kontokotsios, G. Langs, B. H. Menze, T. Salas Fernandez, R. Schaer, A. Walleyo, M. Weber, Y. Dicente Cid, T. Gass, M. Heinrich, F. Jia, F. Kahl, R. Kechichian, D. Mai, A. B. Spanier, G. Vincent, C. Wang, D. Wyeth, and A. Hanbury, "Cloud-based evaluation of anatomical structure segmentation and landmark detection algorithms: Visceral anatomy benchmarks," *IEEE Transactions on Medical Imaging*, vol. 35, no. 11, pp. 2459–2475, Nov 2016.
- [21] A. L. Simpson, M. Antonelli, S. Bakas, M. Bilello, K. Farahani, B. van Ginneken, A. Kopp-Schneider, B. A. Landman, G. J. S. Litjens, B. H. Menze, O. Ronneberger, R. M. Summers, P. Bilic, P. F. Christ, R. K. G. Do, M. Gollub, J. Golia-Pernicka, S. Heckers, W. R. Jarnagin, M. McHugh, S. Napel, E. Vorontsov, L. Maier-Hein, and M. J. Cardoso, "A large annotated medical image dataset for the development and evaluation of segmentation algorithms," *CoRR*, vol. abs/1902.09063, 2019. [Online]. Available: <http://arxiv.org/abs/1902.09063>
- [22] T. N. Ziegenfuss, M. Rogers, L. Lowery, N. Mullins, R. Mendel, J. Antonio, and P. Lemon, "Effect of creatine loading on anaerobic performance and skeletal muscle volume in ncaa division i athletes," *Nutrition*, vol. 18, no. 5, pp. 397 – 402, 2002. [Online]. Available: <http://www.sciencedirect.com/science/article/pii/S0899900701008024>
- [23] A. P. Wroblewski, F. Amati, M. A. Smiley, B. Goodpaster, and V. Wright, "Chronic exercise preserves lean muscle mass in masters athletes," *The Physician and Sportsmedicine*, vol. 39, no. 3, pp. 172–178, 2011, pMID: 22030953. [Online]. Available: <https://doi.org/10.3810/psm.2011.09.1933>
- [24] E. L. Finanger, B. Russman, S. C. Forbes, W. D. Rooney, G. A. Walter, and K. Vandenborne, "Use of skeletal muscle mri in diagnosis and monitoring disease progression in duchenne muscular dystrophy," *Physical Medicine and Rehabilitation Clinics of North America*, vol. 23, no. 1, pp. 1 – 10, 2012, recent Advancements in Neuromuscular Medicine. [Online]. Available: <http://www.sciencedirect.com/science/article/pii/S1047965111001033>
- [25] B. Hiba, N. Richard, L. J. Hbert, C. Cot, M. Nejari, C. Vial, F. Bouhour, J. Puymirat, and M. Janier, "Quantitative assessment of skeletal muscle degeneration in patients with myotonic dystrophy type 1 using mri," *Journal of Magnetic Resonance Imaging*, vol. 35, no. 3, pp. 678–685, 2012. [Online]. Available: <https://onlinelibrary.wiley.com/doi/abs/10.1002/jmri.22849>
- [26] S. Ghosh, P. Boulanger, S. T. Acton, S. S. Blemker, and N. Ray, "Automated 3d muscle segmentation from mri data using convolutional neural network," in *2017 IEEE International Conference on Image Processing (ICIP)*. IEEE, 2017, pp. 4437–4441.
- [27] E. Ahmad, J. S. McPhee, H. Degens, and M. H. Yap, "Automatic segmentation of mri human thigh muscles: Combination of reliable and fast framework methods for quadriceps, femur and marrow segmentation," in *Proceedings of the 2018 8th International Conference on Biomedical Engineering and Technology*, ser. ICBET '18. New York, NY, USA: ACM, 2018, pp. 31–38. [Online]. Available: <http://doi.acm.org/10.1145/3208955.3208958>
- [28] I. Wolf, M. Vetter, I. Wegner, T. Buttger, M. Nolden, M. Schbinger, M. Hastenteufel, T. Kunert, and H.-P. Meinzer, "The medical imaging interaction toolkit," *Medical Image Analysis*, vol. 9, no. 6, pp. 594 – 604, 2005, iTK. [Online]. Available: <http://www.sciencedirect.com/science/article/pii/S1361841505000344>
- [29] C. F. Baumgartner, L. M. Koch, M. Pollefeys, and E. Konukoglu, "An exploration of 2D and 3D deep learning techniques for cardiac MR image segmentation," *CoRR*, vol. abs/1709.04496, 2017. [Online]. Available: <http://arxiv.org/abs/1709.04496>
- [30] X. Glorot and Y. Bengio, "Understanding the difficulty of training deep feedforward neural networks," in *Proceedings of the thirteenth international conference on artificial intelligence and statistics*, 2010, pp. 249–256.
- [31] D. P. Kingma and J. Ba, "Adam: A method for stochastic optimization," in *3rd International Conference on Learning Representations, ICLR 2015, San Diego, CA, USA, May 7-9, 2015, Conference Track Proceedings*, Y. Bengio and Y. LeCun, Eds., 2015. [Online]. Available: <http://arxiv.org/abs/1412.6980>
- [32] N. Abraham and N. M. Khan, "A novel focal tv loss function with improved attention U-Net for lesion segmentation," *CoRR*, vol. abs/1810.07842, 2018. [Online]. Available: <http://arxiv.org/abs/1810.07842>
- [33] O. Oktay, J. Schlemper, L. L. Folgoc, M. C. H. Lee, M. P. Heinrich, K. Misawa, K. Mori, S. G. McDonagh, N. Y. Hammerla, B. Kainz, B. Glocker, and D. Rueckert, "Attention U-Net: Learning where to look for the pancreas," *CoRR*, vol. abs/1804.03999, 2018. [Online]. Available: <http://arxiv.org/abs/1804.03999>
- [34] K. Kamnitsas, C. Ledig, V. F. Newcombe, J. P. Simpson, A. D. Kane, D. K. Menon, D. Rueckert, and B. Glocker, "Efficient multi-scale 3d cnn with fully connected crf for accurate brain lesion segmentation," *Medical Image Analysis*, vol. 36, pp. 61 – 78, 2017. [Online]. Available: <http://www.sciencedirect.com/science/article/pii/S1361841516301839>
- [35] J. Dolz, K. Gopinath, J. Yuan, H. Lombaert, C. Desrosiers, and I. Ben Ayed, "Hyperdense-net: A hyper-densely connected cnn for multi-modal image segmentation," *IEEE Transactions on Medical Imaging*, vol. 38, no. 5, pp. 1116–1126, May 2019.
- [36] A. Zhao, G. Balakrishnan, F. Durand, J. V. Guttag, and A. V. Dalca, "Data augmentation using learned transformations for one-shot medical image segmentation," in *The IEEE Conference on Computer Vision and Pattern Recognition (CVPR)*, June 2019.
- [37] A. Tversky, "Features of similarity," *Psychological Review*, vol. 84, no. 4, pp. 327–352, 1977. [Online]. Available: <https://doi.org/10.1037/0033-295x.84.4.327>
- [38] A. Ghosh, H. Kumar, and P. Sastry, "Robust loss functions under label noise for deep neural networks," in *Thirty-First AAAI Conference on Artificial Intelligence*, 2017.
- [39] F. Isensee, J. Petersen, A. Klein, D. Zimmerer, P. F. Jaeger, S. Kohl, J. Wasserthal, G. Koehler, T. Norajitra, S. J. Wirkert, and K. H. Maier-Hein, "nnU-Net: Self-adapting framework for U-Net-based medical image segmentation," *CoRR*, vol. abs/1809.10486, 2018. [Online]. Available: <http://arxiv.org/abs/1809.10486>
- [40] M. Khened, V. A. Kollerathu, and G. Krishnamurthi, "Fully convolutional multi-scale residual densenets for cardiac segmentation and automated cardiac diagnosis using ensemble of classifiers," *Medical image analysis*, vol. 51, pp. 21–45, 2019.

S1. SUPPLEMENTARY MATERIALS

A. Overview of supervised semantic segmentation

From an input feature image $\mathbf{x} = \{x_m\}$, a CNN classifier $f(\mathbf{x}, \boldsymbol{\theta})$ estimates the per-class probability $\mathbf{p} = \{p_m^c\}$ that x_m should be assigned the ground-truth label class c :

$$p_m^c = \mathbb{P}(y_m = c \mid \mathbf{x}, \boldsymbol{\theta}) \quad (\text{S1})$$

from which the predicted label map $\hat{\mathbf{y}} = \{\hat{y}_m\}$ is generated:

$$\hat{y}_m = \operatorname{argmax}_c p_m^c \quad (\text{S2})$$

CNN classifier training may take multiple forms, which include supervised learning when there exists a training dataset $D_{train} = \{(\mathbf{x}, \mathbf{y})_n\}$, $n \in \{1, \dots, N\}$ with N annotated image pairs (\mathbf{x}, \mathbf{y}) . This involves optimizing the model parameters $\boldsymbol{\theta}$ to minimize the value of a selected loss function $J(\boldsymbol{\theta})$, often by back-propagating the gradient $\frac{dJ}{d\boldsymbol{\theta}}$ with some variant of the gradient decent algorithm.

Loss function essentially measures difference between the ground-truth label & current predictions, and is often chosen based on the problem in hand. In solving classification problems, it is common to start with crossentropy loss:

$$J_{xent}(\boldsymbol{\theta}) = - \sum_m^M \sum_c^C y_m^c \log p_m^c \quad (\text{S3})$$

Meanwhile, performance of CNN classifier in semantic segmentation is often evaluated using some form of intersection-over-union (IOU) matrix. It is hence intuitive to select IOU-derived losses for semantic segmentation problems. One popular option is the soft dice loss [4]:

$$J_{dice_{soft}}(\boldsymbol{\theta}) = \sum_c^C (1 - \text{softdice}^c) \quad (\text{S4})$$

which is derived from the soft dice score for every class c :

$$\text{softdice}^c = \frac{2 \cdot \sum_m^M (y_m^c \cdot p_m^c)}{\sum_m^M y_m^c + \sum_m^M p_m^c} \quad (\text{S5})$$

Minimizing the soft dice loss is effectively equivalent to maximizing the IOU-based soft dice score. Intuitively, other loss functions derived in a similar manner should also achieve the same effect, such as minimizing the negative log of the soft dice score:

$$J_{dice_{log}}(\boldsymbol{\theta}) = - \sum_c^C \log \text{softdice}^c \quad (\text{S6})$$

With both crossentropy and soft dice loss coming with their own strengths and weaknesses, some studies adopt a merged version of the two losses [39], [40]:

$$J_{xentdice}(\boldsymbol{\theta}) = a \cdot J_{xent}(\boldsymbol{\theta}) + b \cdot J_{dice}(\boldsymbol{\theta}) \quad (\text{S7})$$

with a and b controlling relative contribution of the two loss components.

B. Dataset details and full evaluation results

TABLE S1: Detail of human thigh and calf datasets

| dataset | dimensions | resolutions (mm) | count | image content |
|-------------|----------------|--------------------|-------|---------------|
| calf-muscle | (384, 308, 44) | (0.47, 0.47, 3.00) | 18 | single calf |
| calf-muscle | (384, 308, 88) | (0.47, 0.47, 1.00) | 4 | single calf |
| calf-tissue | (704, 496, 25) | (0.54, 0.54, 7.00) | 42 | both calves |
| thigh | (512, 512, 32) | (0.39, 0.39, 5.00) | 40 | single thigh |

TABLE S2: Full result of Section IV-A. This is an extension of Table I in the main text, with dice scores for the tumor label classes, as well as classifiers trained using images sliced in the coronal and sagittal directions.

| plane | label_class classifier_type loss_function | average | | liver | | pancreas | | spleen | | liver_tumor | | pancreas_tumor | |
|----------|---|---------------|---------------|---------------|---------------|---------------|---------------|---------------|---------------|---------------|---------------|----------------|---------------|
| | | generic | specific | generic | specific | generic | specific | generic | specific | generic | specific | generic | specific |
| axial | $dice_{soft}$ | 0.0316 | 0.0308 | 0.0000 | 0.0000 | 0.0043 | 0.0000 | 0.0000 | 0.0000 | 0.1538 | 0.1538 | 0.0000 | 0.0000 |
| | $dice_{soft}(w/o\ empty)$ | 0.2595 | 0.4677 | 0.0000 | 0.8606 | 0.5254 | 0.5153 | 0.7684 | 0.8089 | 0.0037 | 0.1538 | 0.0000 | 0.0000 |
| | $dice_{log}$ | 0.1485 | 0.3571 | 0.2278 | 0.8244 | 0.2672 | 0.1606 | 0.0925 | 0.7702 | 0.1538 | 0.0300 | 0.0009 | 0.0004 |
| | $xent_{base}$ | 0.0642 | 0.6198 | 0.1717 | 0.9064 | 0.0475 | 0.6919 | 0.0251 | 0.8973 | 0.0642 | 0.4849 | 0.0126 | 0.1185 |
| | $xent_{base}+0.1 * dice_{soft}$ | 0.4885 | 0.5227 | 0.6047 | 0.8857 | 0.6408 | 0.6641 | 0.8202 | 0.8907 | 0.3767 | 0.1732 | 0.0002 | 0.0000 |
| | $xent_{base}+dice_{log}$ | 0.5673 | 0.6040 | 0.8423 | 0.8915 | 0.5933 | 0.5963 | 0.8556 | 0.8977 | 0.4070 | 0.4933 | 0.1385 | 0.1411 |
| | $xent_{or}$ | 0.6116 | 0.5777 | 0.9049 | 0.9045 | 0.6845 | 0.6209 | 0.8662 | 0.8121 | 0.4475 | 0.4341 | 0.1551 | 0.1169 |
| | $xent_{or}+0.1 * dice_{soft}$ | 0.6024 | 0.6165 | 0.8980 | 0.9023 | 0.6860 | 0.6869 | 0.8605 | 0.9005 | 0.4044 | 0.4851 | 0.1629 | 0.1078 |
| | $xent_{or}+dice_{log}$ | 0.6071 | 0.5895 | 0.9018 | 0.8976 | 0.6419 | 0.6222 | 0.8662 | 0.8198 | 0.4718 | 0.4791 | 0.1539 | 0.1289 |
| | $xent_{plus}$ | 0.6191 | 0.6073 | 0.9097 | 0.9080 | 0.6619 | 0.6735 | 0.8890 | 0.8506 | 0.4437 | 0.4450 | 0.1911 | 0.1592 |
| | $xent_{plus}+0.1 * dice_{soft}$ | 0.6105 | 0.5780 | 0.8944 | 0.9063 | 0.6985 | 0.6716 | 0.9009 | 0.8851 | 0.4097 | 0.4164 | 0.1490 | 0.0106 |
| | $xent_{plus}+dice_{log}$ | 0.6105 | 0.6076 | 0.8989 | 0.9060 | 0.6528 | 0.6493 | 0.8421 | 0.8821 | 0.4521 | 0.4742 | 0.2065 | 0.1265 |
| coronal | $dice_{soft}$ | 0.1531 | 0.0308 | 0.0000 | 0.0000 | 0.0000 | 0.0000 | 0.7618 | 0.0000 | 0.0039 | 0.1538 | 0.0000 | 0.0000 |
| | $dice_{soft}(w/o\ empty)$ | 0.3342 | 0.4512 | 0.3511 | 0.8505 | 0.4809 | 0.4687 | 0.8360 | 0.7828 | 0.0032 | 0.1538 | 0.0000 | 0.0000 |
| | $dice_{log}$ | 0.2118 | 0.3860 | 0.3083 | 0.7083 | 0.3554 | 0.4021 | 0.2414 | 0.7387 | 0.1538 | 0.0654 | 0.0000 | 0.0156 |
| | $xent_{base}$ | 0.0978 | 0.5273 | 0.0750 | 0.8674 | 0.0336 | 0.6144 | 0.2468 | 0.7983 | 0.1149 | 0.3181 | 0.0184 | 0.0384 |
| | $xent_{base}+0.1 * dice_{soft}$ | 0.3335 | 0.5499 | 0.1623 | 0.8856 | 0.4378 | 0.5981 | 0.8352 | 0.8174 | 0.2323 | 0.4085 | 0.0002 | 0.0399 |
| | $xent_{base}+dice_{log}$ | 0.5113 | 0.4929 | 0.7909 | 0.8238 | 0.5413 | 0.4829 | 0.8349 | 0.7866 | 0.3189 | 0.3461 | 0.0706 | 0.0255 |
| | $xent_{or}$ | 0.5221 | 0.5150 | 0.8734 | 0.8775 | 0.5379 | 0.5675 | 0.8311 | 0.7950 | 0.3137 | 0.2872 | 0.0542 | 0.0480 |
| | $xent_{or}+0.1 * dice_{soft}$ | 0.5483 | 0.5561 | 0.8701 | 0.8552 | 0.6263 | 0.6175 | 0.8663 | 0.8624 | 0.3188 | 0.3843 | 0.0601 | 0.0610 |
| | $xent_{or}+dice_{log}$ | 0.5130 | 0.5217 | 0.8229 | 0.8574 | 0.5544 | 0.5550 | 0.7868 | 0.8400 | 0.2970 | 0.3049 | 0.1039 | 0.0513 |
| | $xent_{plus}$ | 0.5461 | 0.5141 | 0.8570 | 0.8598 | 0.6319 | 0.5949 | 0.8516 | 0.7877 | 0.3039 | 0.2723 | 0.0861 | 0.0557 |
| | $xent_{plus}+0.1 * dice_{soft}$ | 0.5476 | 0.5369 | 0.8593 | 0.8744 | 0.6212 | 0.5538 | 0.9001 | 0.8831 | 0.3119 | 0.3640 | 0.0455 | 0.0091 |
| | $xent_{plus}+dice_{log}$ | 0.4978 | 0.5183 | 0.8409 | 0.8213 | 0.5793 | 0.5603 | 0.7906 | 0.7923 | 0.2027 | 0.3718 | 0.0754 | 0.0456 |
| sagittal | $dice_{soft}$ | 0.0240 | 0.0308 | 0.0000 | 0.0000 | 0.0047 | 0.0000 | 0.0000 | 0.0000 | 0.1154 | 0.1538 | 0.0000 | 0.0000 |
| | $dice_{soft}(w/o\ empty)$ | 0.3265 | 0.3904 | 0.3554 | 0.7991 | 0.5387 | 0.5254 | 0.7351 | 0.4736 | 0.0031 | 0.1538 | 0.0000 | 0.0000 |
| | $dice_{log}$ | 0.1737 | 0.3154 | 0.2026 | 0.5913 | 0.2946 | 0.4804 | 0.2927 | 0.4285 | 0.0787 | 0.0570 | 0.0000 | 0.0199 |
| | $xent_{base}$ | 0.0663 | 0.5397 | 0.1111 | 0.8164 | 0.0133 | 0.6631 | 0.0749 | 0.8138 | 0.1241 | 0.3412 | 0.0084 | 0.0639 |
| | $xent_{base}+0.1 * dice_{soft}$ | 0.3734 | 0.4987 | 0.1828 | 0.8329 | 0.5870 | 0.6284 | 0.7780 | 0.6854 | 0.3187 | 0.3467 | 0.0003 | 0.0000 |
| | $xent_{base}+dice_{log}$ | 0.4680 | 0.4806 | 0.7341 | 0.7357 | 0.5168 | 0.5755 | 0.7514 | 0.7664 | 0.2781 | 0.2076 | 0.0598 | 0.1178 |
| | $xent_{or}$ | 0.5201 | 0.5177 | 0.7815 | 0.7573 | 0.6083 | 0.5909 | 0.8127 | 0.9061 | 0.3489 | 0.2740 | 0.0491 | 0.0601 |
| | $xent_{or}+0.1 * dice_{soft}$ | 0.5557 | 0.4907 | 0.8219 | 0.7640 | 0.6329 | 0.6364 | 0.8486 | 0.7010 | 0.3155 | 0.3522 | 0.1598 | 0.0000 |
| | $xent_{or}+dice_{log}$ | 0.4932 | 0.4895 | 0.7415 | 0.7382 | 0.6162 | 0.6284 | 0.7933 | 0.7693 | 0.2548 | 0.2250 | 0.0602 | 0.0863 |
| | $xent_{plus}$ | 0.5170 | 0.5310 | 0.7849 | 0.7842 | 0.6417 | 0.6293 | 0.7873 | 0.8363 | 0.2854 | 0.3317 | 0.0859 | 0.0735 |
| | $xent_{plus}+0.1 * dice_{soft}$ | 0.5670 | 0.5215 | 0.8221 | 0.7623 | 0.6398 | 0.6412 | 0.8598 | 0.8743 | 0.3554 | 0.3270 | 0.1581 | 0.0029 |
| | $xent_{plus}+dice_{log}$ | 0.4845 | 0.5146 | 0.6935 | 0.7143 | 0.5997 | 0.6521 | 0.7929 | 0.8340 | 0.2523 | 0.2867 | 0.0842 | 0.0861 |

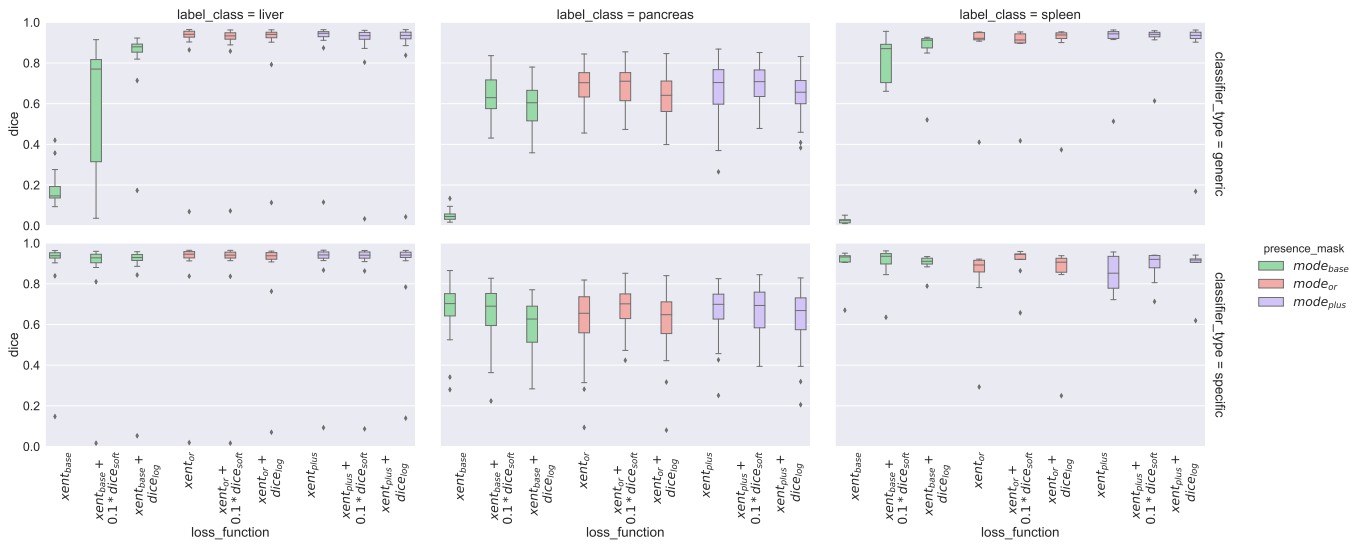


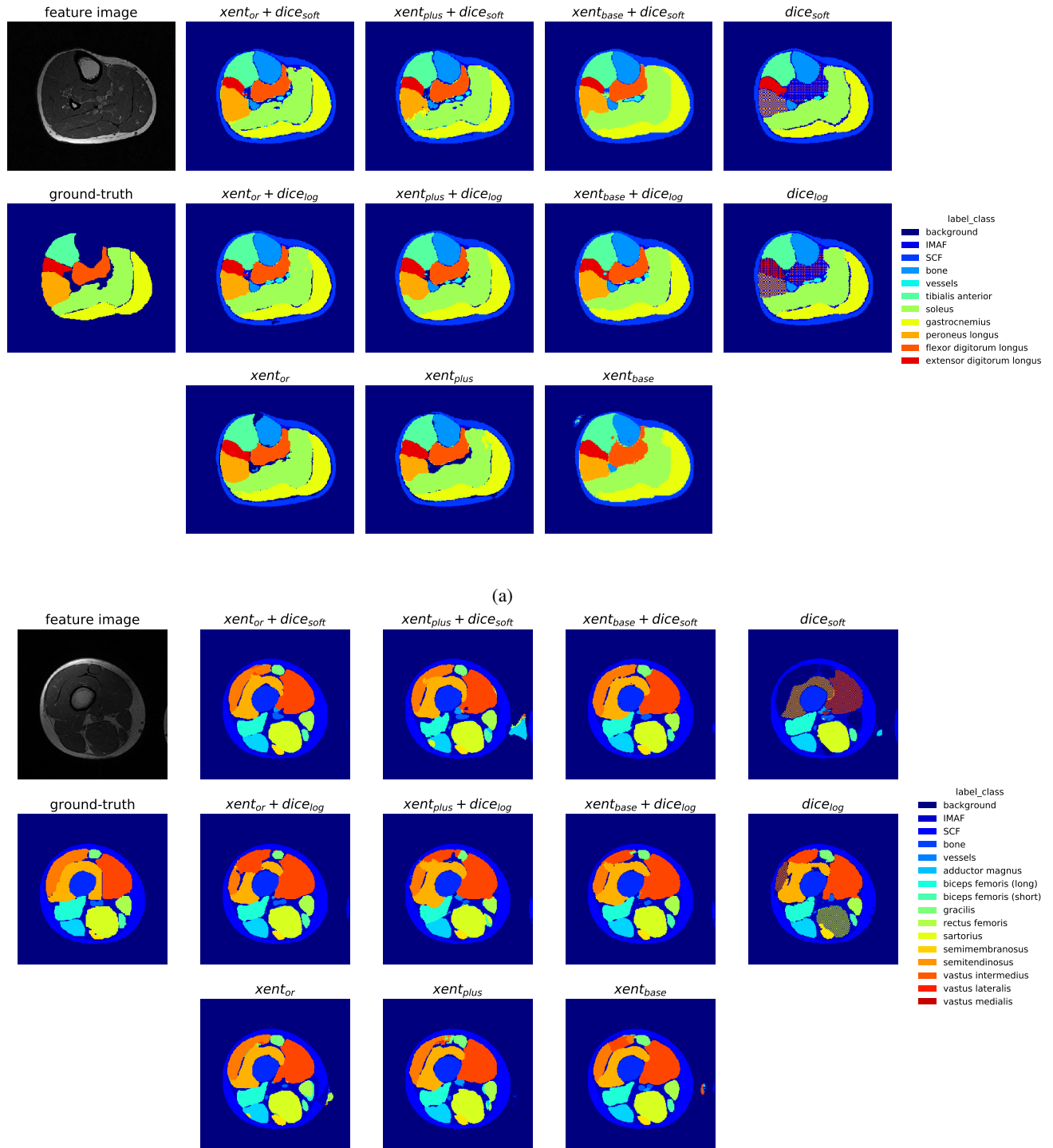
Fig. S1: Box and whisker plots of the result from Table S2. Dice performances of the specific-/generic-classifier pairs are plotted against the loss function they are trained with. Loss functions without any crossentropy component are omitted due to poor performance

TABLE S3: Dice performance of the specific- and generic-classifiers on D_{test} as size of the training set D_{train} shrinks from 80% to 2.5%. Dice scores in bold correspond to the best performing loss function in each combination of D_{train} size, classifier type (generic or specific), and label class.

| label_class | classifier_type train_percent loss_function | generic | | | | | | specific | | | | | |
|-------------|---|---------------|---------------|---------------|---------------|---------------|---------------|---------------|---------------|---------------|---------------|---------------|---------------|
| | | 2.5 | 5 | 10 | 20 | 40 | 80 | 2.5 | 5 | 10 | 20 | 40 | 80 |
| average | $xent_{base}$ | - | - | - | - | - | - | 0.4921 | 0.5405 | 0.6597 | 0.7088 | 0.7282 | 0.8319 |
| | $xent_{base} + 0.1 * dice_{soft}$ | - | - | - | - | - | - | 0.4433 | 0.5613 | 0.7046 | 0.6940 | 0.7686 | 0.8135 |
| | $xent_{base} + dice_{log}$ | - | - | - | - | - | - | 0.3401 | 0.5040 | 0.6762 | 0.6492 | 0.7204 | 0.7952 |
| | $xent_{plus}$ | 0.5027 | 0.6065 | 0.6770 | 0.7614 | 0.7883 | 0.8202 | 0.4505 | 0.5648 | 0.6122 | 0.7052 | 0.7531 | 0.8107 |
| | $xent_{or} + 0.1 * dice_{soft}$ | 0.4480 | 0.5972 | 0.6731 | 0.7183 | 0.8026 | 0.8148 | 0.4933 | 0.6010 | 0.6988 | 0.7335 | 0.8041 | 0.8299 |
| | $xent_{or} + dice_{log}$ | 0.5268 | 0.6258 | 0.6904 | 0.7341 | 0.7644 | 0.8033 | - | - | - | - | - | - |
| | $xent_{plus} + 0.1 * dice_{soft}$ | 0.4512 | 0.5719 | 0.6887 | 0.7375 | 0.8116 | 0.8313 | - | - | - | - | - | - |
| | $xent_{plus} + dice_{log}$ | 0.4928 | 0.6252 | 0.6706 | 0.7404 | 0.7852 | 0.7979 | - | - | - | - | - | - |
| liver | $xent_{base}$ | - | - | - | - | - | - | 0.7632 | 0.8380 | 0.8568 | 0.8681 | 0.8740 | 0.9064 |
| | $xent_{base} + 0.1 * dice_{soft}$ | - | - | - | - | - | - | 0.7391 | 0.8331 | 0.8793 | 0.8860 | 0.8856 | 0.8857 |
| | $xent_{base} + dice_{log}$ | - | - | - | - | - | - | 0.8095 | 0.7681 | 0.8579 | 0.8656 | 0.8766 | 0.8915 |
| | $xent_{plus}$ | 0.8170 | 0.8633 | 0.8729 | 0.8918 | 0.8974 | 0.9097 | 0.7559 | 0.8546 | 0.8240 | 0.8830 | 0.9003 | 0.9080 |
| | $xent_{or} + 0.1 * dice_{soft}$ | 0.6837 | 0.8528 | 0.8582 | 0.8686 | 0.8879 | 0.8980 | 0.8136 | 0.8553 | 0.8835 | 0.8856 | 0.8950 | 0.9023 |
| | $xent_{or} + dice_{log}$ | 0.7282 | 0.8171 | 0.8302 | 0.8810 | 0.8706 | 0.9018 | - | - | - | - | - | - |
| | $xent_{plus} + 0.1 * dice_{soft}$ | 0.7502 | 0.8292 | 0.8570 | 0.8823 | 0.8886 | 0.8944 | - | - | - | - | - | - |
| | $xent_{plus} + dice_{log}$ | 0.7643 | 0.8219 | 0.8621 | 0.8784 | 0.8678 | 0.8989 | - | - | - | - | - | - |
| pancreas | $xent_{base}$ | - | - | - | - | - | - | 0.2835 | 0.3223 | 0.4261 | 0.5542 | 0.6443 | 0.6919 |
| | $xent_{base} + 0.1 * dice_{soft}$ | - | - | - | - | - | - | 0.2412 | 0.3415 | 0.4723 | 0.5225 | 0.5865 | 0.6641 |
| | $xent_{base} + dice_{log}$ | - | - | - | - | - | - | 0.2107 | 0.2950 | 0.3766 | 0.3965 | 0.4834 | 0.5963 |
| | $xent_{plus}$ | 0.1150 | 0.2907 | 0.3832 | 0.5608 | 0.6145 | 0.6619 | 0.2210 | 0.2765 | 0.3643 | 0.4517 | 0.5907 | 0.6735 |
| | $xent_{or} + 0.1 * dice_{soft}$ | 0.0818 | 0.2353 | 0.3914 | 0.5056 | 0.6415 | 0.6860 | 0.2687 | 0.3853 | 0.4391 | 0.5193 | 0.6238 | 0.6869 |
| | $xent_{or} + dice_{log}$ | 0.1883 | 0.3285 | 0.4417 | 0.5347 | 0.5874 | 0.6419 | - | - | - | - | - | - |
| | $xent_{plus} + 0.1 * dice_{soft}$ | 0.0801 | 0.2085 | 0.4547 | 0.5718 | 0.6419 | 0.6985 | - | - | - | - | - | - |
| | $xent_{plus} + dice_{log}$ | 0.0900 | 0.3356 | 0.3805 | 0.5735 | 0.6236 | 0.6528 | - | - | - | - | - | - |
| spleen | $xent_{base}$ | - | - | - | - | - | - | 0.4295 | 0.4611 | 0.6961 | 0.7041 | 0.6663 | 0.8973 |
| | $xent_{base} + 0.1 * dice_{soft}$ | - | - | - | - | - | - | 0.3496 | 0.5091 | 0.7621 | 0.6736 | 0.8338 | 0.8907 |
| | $xent_{base} + dice_{log}$ | - | - | - | - | - | - | 0.0000 | 0.4490 | 0.7941 | 0.6855 | 0.8011 | 0.8977 |
| | $xent_{plus}$ | 0.5761 | 0.6657 | 0.7750 | 0.8316 | 0.8531 | 0.8890 | 0.3746 | 0.5632 | 0.6481 | 0.7809 | 0.7681 | 0.8506 |
| | $xent_{or} + 0.1 * dice_{soft}$ | 0.5784 | 0.7034 | 0.7697 | 0.7807 | 0.8783 | 0.8605 | 0.3976 | 0.5624 | 0.7737 | 0.7955 | 0.8933 | 0.9005 |
| | $xent_{or} + dice_{log}$ | 0.6639 | 0.7318 | 0.7993 | 0.7865 | 0.8351 | 0.8622 | - | - | - | - | - | - |
| | $xent_{plus} + 0.1 * dice_{soft}$ | 0.5231 | 0.6780 | 0.7542 | 0.7583 | 0.9044 | 0.9009 | - | - | - | - | - | - |
| | $xent_{plus} + dice_{log}$ | 0.6242 | 0.7182 | 0.7691 | 0.7694 | 0.8643 | 0.8421 | - | - | - | - | - | - |

TABLE S4: Dice performance of classifiers on the calf and thigh datasets. Dice scores in bold correspond to the best performing classifier in each label class. $pl+edl$ represents the pixel-wise union of *peroneus longus* and *extensor digitorum longus*. Performance of calf IMAF could not be evaluated since it is not manually annotated in the calf datasets.

| label_class classifier_type loss_function | SCF | | bone | | vessels | | tibialis anterior | | soleus | | gastrocnemius | | flexor digitorum longus | | peroneus longus | | extensor digitorum longus | | $pl+edl$ | |
|---|---------------|---------------|---------------|---------------|---------------|----------------|-------------------|----------------|---------------|---------------|----------------|---------------|-------------------------|----------------|--------------------|------------------|---------------------------|---------------|---------------|---------------|
| | generic | specific | generic | specific | generic | specific | generic | specific | generic | specific | generic | specific | generic | specific | generic | specific | generic | specific | generic | specific |
| $dice_{soft}$ | 0.8453 | 0.8523 | 0.9334 | 0.9448 | 0.4523 | 0.5820 | 0.8637 | 0.8787 | 0.8578 | 0.9099 | 0.8483 | 0.9146 | 0.2431 | 0.8751 | 0.5247 | 0.8335 | 0.6347 | 0.6231 | 0.6128 | 0.8679 |
| $dice_{log}$ | 0.8564 | 0.8608 | 0.9292 | 0.9338 | 0.5078 | 0.3816 | 0.8760 | 0.4279 | 0.8638 | 0.5314 | 0.8734 | 0.5241 | 0.2752 | 0.6766 | 0.5068 | 0.2645 | 0.4386 | 0.1175 | 0.5485 | 0.3619 |
| $xent_{base}$ | 0.8214 | 0.7515 | 0.8129 | 0.9216 | 0.3430 | 0.4190 | 0.8159 | 0.8109 | 0.8755 | 0.8946 | 0.8769 | 0.9030 | 0.8595 | 0.8841 | 0.8349 | 0.8242 | 0.6664 | 0.6656 | 0.8487 | 0.8557 |
| $xent_{base} + 0.1 * dice_{soft}$ | 0.8331 | 0.8699 | 0.9354 | 0.9247 | 0.4561 | 0.5822 | 0.8455 | 0.8748 | 0.8628 | 0.9068 | 0.8883 | 0.9117 | 0.8706 | 0.8934 | 0.7446 | 0.8223 | 0.5037 | 0.6415 | 0.8140 | 0.8539 |
| $xent_{base} + dice_{log}$ | 0.8585 | 0.8676 | 0.9312 | 0.9397 | 0.5439 | 0.5865 | 0.8702 | 0.8800 | 0.8858 | 0.8903 | 0.9045 | 0.8948 | 0.8926 | 0.8282 | 0.8201 | 0.8177 | 0.6129 | 0.6107 | 0.8296 | 0.8415 |
| $xent_{or}$ | 0.8610 | 0.8610 | 0.9313 | 0.9474 | 0.5017 | 0.5171 | 0.8670 | 0.8914 | 0.8844 | 0.8936 | 0.8841 | 0.8996 | 0.8844 | 0.8865 | 0.8080 | 0.7968 | 0.6320 | 0.6637 | 0.8416 | 0.8378 |
| $xent_{or} + 0.1 * dice_{soft}$ | 0.8331 | 0.8663 | 0.9393 | 0.9480 | 0.5302 | 0.5572 | 0.8319 | 0.8942 | 0.9050 | 0.9007 | 0.8715 | 0.8937 | 0.8762 | 0.8864 | 0.7226 | 0.7878 | 0.5800 | 0.6295 | 0.7834 | 0.8279 |
| $xent_{or} + dice_{log}$ | 0.8555 | 0.8710 | 0.9228 | 0.9455 | 0.5336 | 0.5672 | 0.9029 | 0.8004 | 0.8829 | 0.8426 | 0.8762 | 0.8328 | 0.8869 | 0.8488 | 0.7881 | 0.7817 | 0.7057 | 0.6117 | 0.8412 | 0.8224 |
| $xent_{plus}$ | 0.8519 | 0.8555 | 0.9250 | 0.9482 | 0.4809 | 0.5183 | 0.8411 | 0.8830 | 0.8601 | 0.8982 | 0.8686 | 0.8999 | 0.8610 | 0.8978 | 0.7230 | 0.8095 | 0.6292 | 0.6366 | 0.7605 | 0.8511 |
| $xent_{plus} + 0.1 * dice_{soft}$ | 0.8324 | 0.8607 | 0.9392 | 0.9435 | 0.5231 | 0.5639 | 0.8136 | 0.8954 | 0.8896 | 0.8968 | 0.8601 | 0.8957 | 0.8729 | 0.9034 | 0.7029 | 0.7858 | 0.5793 | 0.6663 | 0.7783 | 0.8328 |
| $xent_{plus} + dice_{log}$ | 0.8709 | 0.8646 | 0.9418 | 0.9472 | 0.5655 | 0.5695 | 0.8332 | 0.8735 | 0.8928 | 0.8983 | 0.9023 | 0.8875 | 0.9026 | 0.8834 | 0.8151 | 0.8343 | 0.6468 | 0.6133 | 0.8635 | 0.8640 |
| label_class classifier_type loss_function | IMAF | SCF | | bone | vessels | biceps femoris | | biceps femoris | | gracilis | rectus femoris | sartorius | semimembranosus | semitendinosus | vastus intermedius | vastus lateralis | vastus medialis | | | |
| | | specific | specific | | | long | short | | | | | | | | | | | | | |
| $dice_{soft}$ | 0.7344 | 0.9453 | 0.9689 | 0.6232 | 0.8325 | 0.8786 | 0.8279 | 0.8254 | 0.0000 | 0.0000 | 0.9014 | 0.0000 | 0.5745 | 0.0000 | 0.6033 | | | | | |
| $dice_{log}$ | 0.7253 | 0.9377 | 0.9674 | 0.4789 | 0.7948 | 0.8429 | 0.7560 | 0.8063 | 0.7131 | 0.8702 | 0.5873 | 0.6815 | 0.8156 | 0.5190 | 0.8387 | | | | | |
| $xent_{base}$ | 0.7015 | 0.9464 | 0.9728 | 0.5712 | 0.8617 | 0.8971 | 0.8200 | 0.8656 | 0.8278 | 0.8997 | 0.9130 | 0.8031 | 0.8515 | 0.8895 | 0.8723 | | | | | |
| $xent_{base} + 0.1 * dice_{soft}$ | 0.7141 | 0.9432 | 0.9726 | 0.5513 | 0.8375 | 0.8733 | 0.7843 | 0.8190 | 0.8122 | 0.8864 | 0.8994 | 0.7811 | 0.8360 | 0.8966 | 0.8911 | | | | | |
| $xent_{base} + dice_{log}$ | 0.7048 | 0.9350 | 0.9590 | 0.4812 | 0.8402 | 0.8734 | 0.7831 | 0.8389 | 0.6542 | 0.8873 | 0.8812 | 0.7929 | 0.8347 | 0.8435 | 0.8638 | | | | | |
| $xent_{or}$ | 0.6911 | 0.9405 | 0.9658 | 0.5220 | 0.8414 | 0.8546 | 0.7799 | 0.8287 | 0.8089 | 0.8523 | 0.8916 | 0.7658 | 0.8402 | 0.8794 | 0.8613 | | | | | |
| $xent_{or} + 0.1 * dice_{soft}$ | 0.7154 | 0.9433 | 0.9721 | 0.5766 | 0.8419 | 0.8657 | 0.8014 | 0.8594 | 0.8373 | 0.8807 | 0.8869 | 0.7888 | 0.8519 | 0.8910 | 0.8987 | | | | | |
| $xent_{or} + dice_{log}$ | 0.7248 | 0.9445 | 0.9718 | 0.5631 | 0.8594 | 0.8738 | 0.7846 | 0.8311 | 0.7540 | 0.9008 | 0.9118 | 0.8218 | 0.8274 | 0.8456 | 0.8672 | | | | | |
| $xent_{plus}$ | 0.6846 | 0.9480 | 0.9317 | 0.4255 | 0.8247 | 0.8479 | 0.7350 | 0.7429 | 0.6899 | 0.8661 | 0.8900 | 0.8248 | 0.8111 | 0.8695 | 0.8488 | | | | | |
| $xent_{plus} + 0.1 * dice_{soft}$ | 0.7107 | 0.9406 | 0.9641 | 0.6142 | 0.8476 | 0.8073 | 0.8142 | 0.8175 | 0.8227 | 0.8822 | 0.8946 | 0.7840 | 0.8604 | 0.8941 | 0.9000 | | | | | |
| $xent_{plus} + dice_{log}$ | 0.7118 | 0.9406 | 0.9635 | 0.4904 | 0.8141 | 0.8843 | 0.7885 | 0.7646 | 0.6694 | 0.8831 | 0.8915 | 0.8184 | 0.8365 | 0.8391 | 0.8668 | | | | | |



(b)

Fig. S2: Label maps predicted by (a) calf generic-classifiers and (b) thigh specific-classifiers.